# Direct mapping of curve-crossing dynamics in IBr by attosecond transient absorption spectroscopy

Yuki Kobayashi,<sup>1\*</sup> Kristina F. Chang,<sup>1</sup> Tao Zeng,<sup>2</sup> Daniel M. Neumark,<sup>1,3\*</sup> Stephen R. Leone<sup>1,3,4\*</sup>

<sup>1</sup>Department of Chemistry, University of California, Berkeley, California 94720, USA

<sup>2</sup>Department of Chemistry, Carleton University, Ottawa, Ontario K1S5B6, Canada

<sup>3</sup>Chemical Sciences Division, Lawrence Berkeley National Laboratory, Berkeley

California 94720, USA

<sup>4</sup>Department of Physics, University of California, Berkeley, California 94720, USA

\*To whom correspondence should be addressed; E-mail: ykoba@berkeley.edu, dneumark@berkeley.edu, srl@berkeley.edu.

The electronic character of photoexcited molecules can abruptly change at avoided crossings and conical intersections. Here, we report direct mapping of the coupled interplay between electrons and nuclei in a prototype molecule, iodine monobromide (IBr), using attosecond transient absorption spectroscopy. A few-femtosecond visible pulse resonantly excites the  $B(^3\Pi_{0^+})$  state of IBr and the accompanying photodissociation dynamics are tracked by an attosecond extreme-ultraviolet pulse that simultaneously probes the I-4d and Br-3d corelevel absorption edges. Direct comparison with quantum mechanical simulations unambiguously identifies the core-level absorption features associated with adiabatic and diabatic channels at the B/Y avoided crossing and concurrent two-photon dissociation processes that involve the Y/Z avoided cross-

ing. The results show clear evidence for rapid switching of valence molecularorbital occupations at the avoided crossing. The conventional picture of a photoexcited molecule smoothly evolving toward a product state on a single potential surface is invalid when degeneracies between neighboring states induce nonadiabatic interactions (1-3). Molecular dynamics that involve avoided crossings and conical intersections have been of fundamental interest in chemical physics since the seminal Landau-Zener model pioneered in the 1930s (4, 5). It is now widely accepted that nonadiabatic interactions play key roles in broad classes of photochemical reactions, such as photoisomerization in the retinal chromophore (6) and photostability of DNA-base pairs against ultraviolet radiation (7). Realization of laser-based control of nonadiabatic processes represents a pivotal milestone in recent progress of spectroscopic studies (8, 9).

Despite these successes, real-time observation of electronic dynamics in nonadiabatic regions remains elusive (10). Conceptually, electronic character can rapidly change in synchrony with nuclear motion. Experimentally, few-femtosecond time resolution is required for the probe, and the intrinsic degeneracy makes it challenging to obtain state-resolved information. Several experimental methods have been applied to this end (11–15), including novel high-harmonic spectroscopy (16) and ultrafast electron diffraction (17). Recent theoretical studies predicted that transient absorption spectroscopy in the x-ray/extreme-ultraviolet (XUV) range offers a unique and powerful route to measure excited-state dynamics around nonadiabatic regions, with core-level absorption capturing the marked reorganization of valence electrons (18, 19). When combined with high-harmonic-generation-based attosecond light sources, this method has the potential to ultimately attain subfemtosecond probing time resolution (20).

Here, we report attosecond transient absorption mapping of valence-electron dynamics accompanying visible-light excitation of iodine monobromide (IBr), a prototype molecule for nonadiabatic photodissociation dynamics (21, 22).. Our primary focus is the switching of electronic character ensuing at an avoided crossing between excited B( $^{3}\Pi_{0^{+}}$ ) and Y(0<sup>+</sup>) states. An outline of the experiment is depicted in Fig. 1A. Photodissociation is triggered by a fewfemtosecond visible-pump pulse ( $\lambda=530$  nm,  $\Delta\lambda=70$  nm, 8 fs, 15  $\mu$ J, Fig. 1B) (23), which selectively excites the neutral electronic states of IBr and minimizes the unfavorable ionization effects that arise in more typical experiments where intense near-infrared excitation is used (24). In the probe step after a delay time  $\tau$ , an attosecond XUV pulse produced by high-harmonic generation is introduced (45-72 eV,  $\sim$ 200 as, Fig. 1C), which encodes the time evolution of the photoexcited molecule in the characteristic core-to-valence absorption signals. A novel feature of the probing scheme is that the XUV-probe pulse simultaneously detects the two core-level absorption edges of IBr, i.e., the N<sub>4,5</sub> edge (4d orbitals) of iodine and the M<sub>4,5</sub> edge (3d orbitals) of bromine, and this enables full tracking of the photofragment electronic states.

Figure 1D shows the potential energy curves of IBr. Multiple avoided crossings are present in diatomic interhalogens because of the strong spin-orbit couplings of the halogen atoms and the absence of q-u symmetry for heteronuclear molecules (21,22). Two physical pictures are invoked to describe the dynamics at avoided crossings (25): in a diabatic picture, electronic states conserve their character as they move along the reaction coordinate, whereas in an adiabatic picture, electronic states are eigenstates of the electronic Hamiltonian and are subject to switching of electronic character. The visible-pump pulse excites the molecule to an attractive  $B(^3\Pi_{0^+})$ state, which undergoes an avoided crossing with a repulsive  $Y(0^+)$  state ( $R_c = 3.3 \text{ Å}$ ). In the diabatic channel at the B/Y avoided crossing (Fig. 1D, inset), the photoexcited molecule remains on the attractive  $B(^3\Pi_{0^+})$  potential conserving its electronic character and evolves toward the spin-orbit excited  $I(^2P_{3/2}) + Br^*(^2P_{1/2})$  asymptote. In the adiabatic channel (Fig. 1D, inset), the photoexcited molecule transfers to the repulsive  $Y(0^+)$  potential rapidly switching its electronic character and proceeds to the ground  $I(^2P_{3/2}) + Br(^2P_{3/2})$  asymptote. The nonadiabatic coupling is of intermediate strength for the B/Y avoided crossing of IBr, and the measured dissociation ratio between the diabatic and adiabatic channels is approximately 3:1 (26). In the experiments, resonance-enhanced two-photon processes are also observed for the visible-pump pulse, which

reaches a peak-field intensity of  $\sim 5 \times 10^{13}$  W/cm<sup>2</sup>. An electronic-structure analysis reveals a large transition dipole moment ( $\sim 3$  Debye) associated with the B  $\rightarrow$  Y transition (24). The Y(0<sup>+</sup>) state undergoes an avoided crossing with the higher Z(0<sup>+</sup>) state ( $R_c = 2.8$  Å), and the dissociation across the Y/Z avoided crossing leads to the I\*( $^2P_{1/2}$ ) + Br( $^2P_{3/2}$ ) asymptote. The B  $\rightarrow$  Z transition is also possible but of less importance ( $\sim 20\%$  compared with B  $\rightarrow$  Y), and is not considered further here.

We first analyze the transient absorption spectrum of the dissociation products (Fig. 2A, recorded at 215-245 fs). The differential optical density ( $\Delta$ OD) is defined as a logarithmic ratio of the transmitted XUV spectra with and without the visible-pump pulse. Iodine and bromine atoms each exhibit three absorption lines in the I  $4d \rightarrow 5p$  and Br  $3d \rightarrow 4p$  series:  ${}^2P_{3/2} \rightarrow {}^2D_{5/2}$  (45.9, 64.5 eV),  ${}^2P_{1/2} \rightarrow {}^2D_{3/2}$  (46.7, 65.1 eV), and  ${}^2P_{3/2} \rightarrow {}^2D_{3/2}$  (47.6, 65.6 eV) (27, 28). In Fig. 2A, the product ratio between the Br and Br\* atoms calculated from the XUV absorption amplitudes is Br\*/Br = 3.3, which is in reasonable agreement with a previous measurement at 525-nm excitation (Br\*/Br = 3.0) (26). At the same time, a sizable signal from the I\* atom is observed, yielding a product ratio of I\*/I = 0.5. The appearance energy of the I\* atom ( $\sim 2.8$  eV) is higher than the center photon energy of the visible-pump pulse ( $\sim 2.3$  eV), thus this signal is attributed to two-photon (or multiphoton) visible-excitation processes. A group of weak absorption signals at 55-58 eV correspond to the I  $4d \rightarrow np$  (n > 5) Rydberg series (29).

Fig. 2B shows transient absorption spectra as a function of delay time. The measurements are carried out from -16 fs to 245 fs delay time at 1.5-fs intervals. To calculate  $\Delta$ OD, the pump-on/pump-off XUV spectra are each averaged over 200 frames (40 laser pulses per frame). The excited-state absorption ( $\Delta$ OD > 0) is shown in bright colors, and the ground-state bleach ( $\Delta$ OD < 0) is shown in gray shades. The observed ground-state bleach features, both in the I-4d and Br-3d windows, exhibit signatures of vibrational coherences in the ground  $X(^1\Sigma_{0^+})$ 

state (isotopic averages:  $\omega_e=268~{\rm cm^{-1}},~\omega_e x_e=0.8~{\rm cm^{-1}},~T=125~{\rm fs})$  (30). In previous studies, vibrational coherences in the neutral ground states launched by strong-field ionization were reported (31, 32). Here, the excitation mechanism is a resonant single-photon process, and unique nodal structures are newly observed in the oscillating absorption signals. We performed quantum wave-packet simulations to compute the core-level absorption spectra, and the observed features are reproduced by taking coherences in the v=0,1, and 2 vibrational states (Fig. S3). The mechanism for the overtone (v=2) excitation is attributed to a stimulated Raman process enhanced by resonant visible-light coupling between the  $X(^1\Sigma_{0^+})$  and  $B(^3\Pi_{0^+})$  states. See supplementary materials for more details (24).

Figures 3A and B show the details of the excited-state absorption in the I-4d and Br-3d windows, respectively. The early-time signals (0-50 fs) exhibit sweeping shifts to lower photon energy, which equates to mapping of the dissociative motion on the  $B(^3\Pi_{0^+})$  potential. The evolution of the photoexcited molecule at the B/Y avoided crossing is encoded in the subsequent temporal window (50-80 fs, dashed boxes), and Figs. 3C and D show the corresponding absorption traces taken at 6-fs intervals (50, 56, 62, 68, 74, and 80 fs). The sharp absorption features associated with the I\*(46.7 eV) and Br\*(65.1 eV) atoms are nearly invariant with respect to delay time. These atomic fragments conceivably originate from two-photon processes that occur on a shorter time scale, and this assignment is corroborated by ab-initio simulations as will be shown later. The other broad signals (denoted by arrows with labels diabatic and adiabatic) exhibit dramatic variations both in the absorption amplitude and energy. As already mentioned, the diabatic channel at the B/Y avoided crossing leads to the I + Br\* asymptote (Fig. 1D) and the associated wave packet conserves its electronic character. In the experimental results of the Br-3d window (Fig. 3D), the absorption signal that exhibits continuous shifts to lower photon energy indeed converges to the Br\* absorption line, and hence it is assigned to the diabatic channel. In the adiabatic channel, on the other hand, the photoexcited molecule changes the electronic character and proceeds to the ground I + Br asymptote (Fig. 1D). In the experimental results (Fig 3D), the Br absorption line suddenly emerges accompanied by no energy shift at a separate photon energy. The discontinuous evolution of the Br signal is a manifestation of the new electronic character acquired from the neighboring  $Y(0^+)$  state. In the I-4d window (Fig. 3C), the XUV absorption signals associated with the diabatic and adiabatic channels are not as widely separated as in the Br-3d window since the same I atom is produced in both channels. Nonetheless, the continuous shifts to lower photon energy and the sudden emergence of the sharp I signal are distinctly resolved, leading to consistent assignments of the B/Y avoided-crossing signals.

To gain more detailed insight into the transitory molecular features, we perform ab-initio simulations of the core-level absorption spectra (24). The valence and core-excited electronic structures are computed by spin-orbit generalized multi-configurational quasi-degenerate perturbation theory (SO-GMC-QDPT) (33, 34), and from these the XUV absorption strengths are obtained. Nonadiabatic dissociation dynamics are simulated fully quantum mechanically by numerically solving the time-dependent Schrödinger equation. The initial wave packets are taken to be in the Franck-Condon region of the  $B(^3\Pi_{0^+})$  state (one-photon process) or on the  $Y(0^+)$  state (two-photon process) to model the relevant visible-light excitations.

Simulated results for the one-photon process are shown in Figs. 3E and F. The sweeping energy shifts in the early-time window are successfully reproduced in the simulation. The  $B(^3\Pi_{0^+})$  state in the Franck-Condon region has a  $[\sigma^2\pi^4\pi^{*3}\sigma^{*1}]$  configuration and is probed by the core-level transitions to the  $\pi^*$  and  $\sigma^*$  orbitals. The observed absorption lines reflect the multiplet structures of the core-excited states that originate from the spin-orbit couplings in the core (I-4d, Br-3d) and valence  $(\pi, \pi^*)$  orbitals (Fig. S6). Some features are broadened and less pronounced in the experiments compared to the simulations, which is attributed to the finite spectral width of the visible-pump pulse and the nuclear wave-packet motion on the

repulsive core-excited potentials. The absorption traces in the temporal window for the B/Y avoided crossing (50-80 fs) are shown in Figs. 3G and H, with assignments of the diabatic and adiabatic channels directly made from the wave-packet simulations. The continuous (diabatic) and discontinuous (adiabatic) evolution of the XUV absorption signals exhibits excellent match with the experiments, providing clear confirmation of the experimental signal assignments at the B/Y avoided crossing.

The origin of the I\* and part of the Br\* signals is verified by the two-photon simulations (Figs. 3I and J). The simulated I\* signal (Fig. 3I) matches the experimental result (Fig. 3A) both in time and absorption energy. Passage through the Y/Z avoided crossing (Fig. 1D) is calculated to occur in  $\sim 25$  fs. These early-time dynamics are not as clearly resolved in the experiments due to the spectral broadening from the fast dissociative motion on the repulsive Y(0<sup>+</sup>) and Z(0<sup>+</sup>) potentials. Calculated absorption strengths of the Y(0<sup>+</sup>) and Z(0<sup>+</sup>) states are provided in Fig. S7 for future reference. The Br\* atom is produced in the two-photon process by way of the wave packet adiabatically transferring from the repulsive Y(0<sup>+</sup>) potential to the attractive B( $^3\Pi_{0^+}$ ) potential at the B/Y avoided crossing. As such, in the simulation, the switching of electronic character causes abrupt emergence of the Br\* signal (Fig. 3J), and the corresponding absorption feature is resolved at  $\sim 40$  fs delay time in the experimental results (Fig. 3B).

To further investigate the electronic-structure information at the B/Y avoided crossing imprinted in the core-level absorption spectra, the orbital energies and electron configurations are examined. Figure 4 shows the energies of the active molecular orbitals as a function of internuclear distance computed at the level of multi-configurational self-consistent field (MCSCF). The energy differences between the core and valence orbitals are closely tied to the observed absorption energies. The exact description of the electronic states requires multi-configurational treatments and inclusion of spin-orbit couplings, as is done in the SO-GMC-QDPT calculations (24). The energies of the I-4d and Br-3d orbitals are nearly invariant throughout the reaction coordi-

nate. This insensitivity to internuclear distance indicates that the observed energy shifts in the diabatic channel (or no shift in the adiabatic channel) reflect the energy variations in the valence orbitals alone. As for the valence orbitals, the energy gradients quantified at the B/Y avoided crossing (gray area) are +1.5 eV/Å and -1.7 eV/Å for  $\sigma$  and  $\sigma^*$ , respectively, but only +0.3eV/Å and -0.2 eV/Å for  $\pi$  and  $\pi^*$ , respectively. These trends indicate that the  $\pi$  and  $\pi^*$  orbitals are effectively no longer contributing to the variation of the potential energies when the wave packet reaches the avoided crossing. A more direct clue to the electronic-character switching is obtained from the electronic configurations computed for each adiabatic state (35–37). Just before the avoided crossing, the B( $^3\Pi_{0^+}$ ) state is a mixed configuration of  $[\sigma^2\pi^4\pi^{*3}\sigma^{*1}]$  and  $[\sigma^2\pi^3\pi^{*4}\sigma^{*1}]$ ; a single vacancy lies in  $\sigma^*$ , and the other vacancy is distributed between  $\pi$  and  $\pi^*$ . After the photoexcited molecule adiabatically transfers to the repulsive  $Y(0^+)$  potential, the main configuration changes to  $[\sigma^2\pi^3\pi^{*3}\sigma^{*2}]$ , where the  $\sigma^*$  orbital is fully occupied and the two vacancies lie in the  $\pi$  and  $\pi^*$  orbitals. A physical picture is drawn from these results, that is, the vacancy in the valence orbitals switches from  $\sigma^*$  to  $\pi/\pi^*$  at the B/Y avoided crossing, giving rise to new core-level absorption signals with no further energy shifts, reflecting the energy invariance of the  $\pi$  and  $\pi^*$  orbitals versus internuclear distance.

The role of the B/Y avoided crossing in the visible-band dynamics of IBr is usually measured via the final product ratio of Br and Br\*. Here, the attosecond XUV probe enables direct mapping of the valence-electron dynamics during the passage through the avoided crossing, with core-level absorption sensitively encoding the energies and occupations of the individual valence orbitals. The valence-electronic structure not only determines the strength of chemical bonds, but also governs the reactivity of a molecule as represented by the frontier-orbital theory; unraveling the radical evolution of valence-electronic structures around nonadiabatic regions will extend the knowledge of photochemical reactions to a new frontier. Application of ultrafast x-ray/XUV light sources in the explorations of chemical dynamics is an actively

advancing field of research (38, 39), and the present results serve as a valuable benchmark for future studies.

### References

- 1. G. A. Worth, L. S. Cederbaum, Annual Review of Physical Chemistry 55, 127 (2004).
- 2. B. G. Levine, T. J. Martínez, Annual Review of Physical Chemistry 58, 613 (2007).
- 3. M. P. Bircher, et al., Structural Dynamics 4, 061510 (2017).
- 4. L. D. Landau, *Phys. Z. Sowjetunion* **2**, 46 (1932).
- 5. C. Zener, R. H. Fowler, R. Soc. London Ser. A 137, 696 (1932).
- 6. D. Polli, et al., Nature 467, 440 (2010).
- 7. T. Schultz, et al., Science **306**, 1765 (2004).
- 8. B. J. Sussman, D. Townsend, M. Y. Ivanov, A. Stolow, Science 314, 278 (2006).
- 9. M. E. Corrales, et al., Nature Chemistry **6**, 785 (2014).
- 10. S. R. Leone, et al., Nature Photonics 8, 162 (2014).
- 11. S. Takeuchi, et al., Science **322**, 1073 (2008).
- 12. M. C. E. Galbraith, et al., Nature Communications 8, 1018 (2017).
- 13. A. von Conta, et al., Nature Communications 9, 3162 (2018).
- 14. A. E. Boguslavskiy, et al., The Journal of Chemical Physics 148, 164302 (2018).
- 15. H. Timmers, et al. (Submitted).
- 16. H. J. Wörner, et al., Science 334, 208 (2011).
- 17. J. Yang, et al., Science **361**, 64 (2018).

- 18. S. P. Neville, et al., Faraday Discuss. 194, 117 (2016).
- S. P. Neville, M. Chergui, A. Stolow, M. S. Schuurman, *Phys. Rev. Lett.* 120, 243001 (2018).
- 20. F. Krausz, M. Ivanov, Rev. Mod. Phys. 81, 163 (2009).
- 21. M. S. Child, R. B. Bernstein, *The Journal of Chemical Physics* **59**, 5916 (1973).
- 22. M. S. Child, *Molecular Physics* **32**, 1495 (1976).
- 23. D. J. Seery, D. Britton, The Journal of Physical Chemistry 68, 2263 (1964).
- 24. See supplementary materials.
- 25. T. Van Voorhis, et al., Annual Review of Physical Chemistry 61, 149 (2010).
- 26. E. Wrede, et al., The Journal of Chemical Physics 114, 2629 (2001).
- 27. L. Nahon, P. Morin, F. C. Farnoux, *Physica Scripta* **1992**, 104 (1992).
- 28. G. O'Sullivan, C. McGuinness, J. T. Costello, E. T. Kennedy, B. Weinmann, *Phys. Rev. A* 53, 3211 (1996).
- 29. L. Nahon, P. Morin, *Phys. Rev. A* **45**, 2887 (1992).
- 30. R. E. Willis, W. W. Clark, The Journal of Chemical Physics 72, 4946 (1980).
- 31. E. R. Hosler, S. R. Leone, Phys. Rev. A 88, 023420 (2013).
- 32. Z. Wei, et al., Nature Communications **8**, 735 (2017).
- 33. T. Zeng, *The Journal of Chemical Physics* **146**, 144103 (2017).

- 34. Y. Kobayashi, T. Zeng, D. M. Neumark, S. R. Leone, *Structural Dynamics* 6, 014101 (2019).
- 35. S. Patchkovskii, *Phys. Chem. Chem. Phys.* **8**, 926 (2006).
- 36. R. Li, et al., Journal of Quantitative Spectroscopy and Radiative Transfer 133, 271 (2014).
- 37. T. Matsuoka, S. Yabushita, The Journal of Physical Chemistry A 119, 9609 (2015).
- 38. M. Chergui, A. H. Zewail, *ChemPhysChem* **10**, 28 (2009).
- 39. P. M. Kraus, M. Zürch, S. K. Cushing, D. M. Neumark, S. R. Leone, *Nature Reviews Chemistry* **2**, 82 (2018).

## Acknowledgments

**Funding:** This work, Y.K., and K.F.C were supported by the National Science Foundation (NSF) (No. CHE-1660417). Y.K., K.F.C., D.M.N., and S.R.L. also acknowledge the funding from the US Army Research Office (ARO) (No. W911NF-14-1-0383). T.Z. acknowledges the Natural Sciences and Engineering Research Council (NSERC) of Canada for research funding (No. RGPIN-2016-06276) and also Carleton University for start-up Grant (No. 186853). Some of the computations by Y.K. were performed using workstations at the Molecular Graphics and Computation Facility (MGCF) at UC Berkeley, which is supported by the National Institutes of Health (NIH) (Grant No. S10OD023532). Y.K. also acknowledges financial support from the Funai Overseas Scholarship.

**Author contributions:** Y.K., D.M.N., and S.R.L. conceived the experiments. Y.K. and K.F.C. performed the attosecond transient absorption measurements. T.Z. developed the SO-GMC-QDPT code. Y.K. performed the electronic-structure calculations and quantum-mechanical simulations. Y.K. analyzed the results and wrote the manuscript with inputs from all authors.

**Competing interests:** The authors declare no competing interests.

**Data and materials availability:** All data is available in the manuscript or the supplementary materials.

# **Supplementary Materials**

Materials and Methods

Supplementary Text

Figs. S1 to S8

Tables S1 and S2

References (40-58)

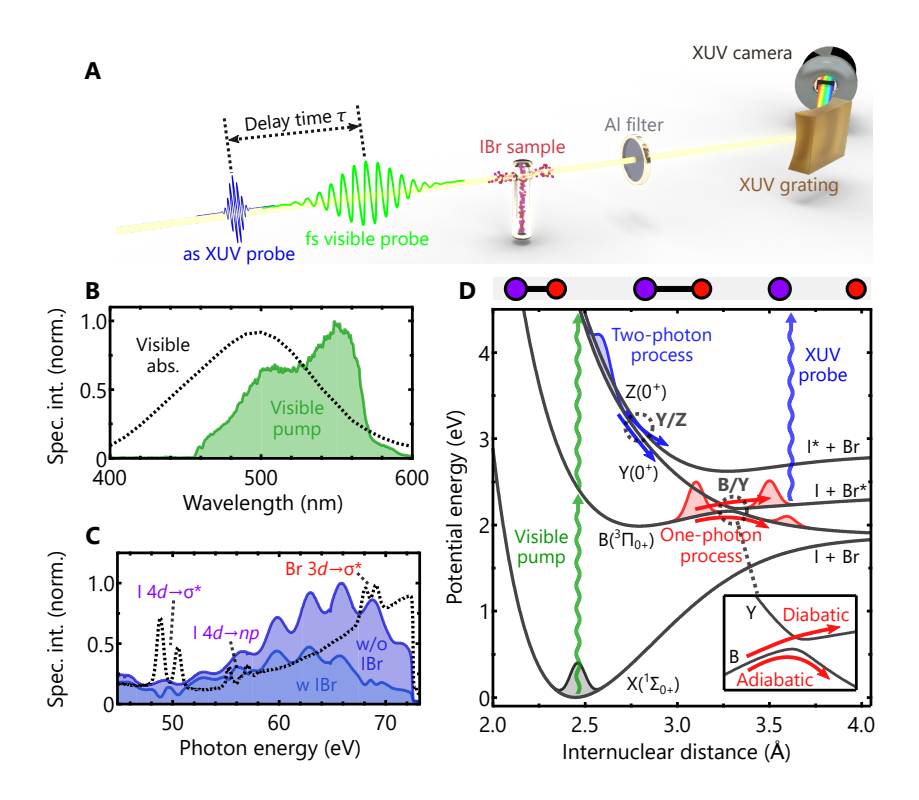


Fig 1: Outline of experiment. (A) Illustration of the experimental setup. (B) Spectrum of the visible-pump pulse (green area), and visible-absorption band of IBr (black dashed curve) (23). (C) Spectra of the XUV-probe pulse recorded with (dark blue area) and without (light blue area) the IBr sample, and the optical density (black dashed curve) calculated from the two spectra. The I-4d and Br-3d edges are covered by the broadband XUV spectrum. (D) Adiabatic potential energy curves of IBr, with the visible and XUV excitation pathways marked by vertical arrows. The red and blue wave packets represent the dissociation pathways from one-photon and two-photon processes, respectively. Avoided crossings are formed between the B and Y states ( $R_c = 3.3 \text{ Å}$ ) and Z and Y states ( $R_c = 2.8 \text{ Å}$ ). The inset shows the adiabatic and diabatic channels at the B/Y avoided crossing.

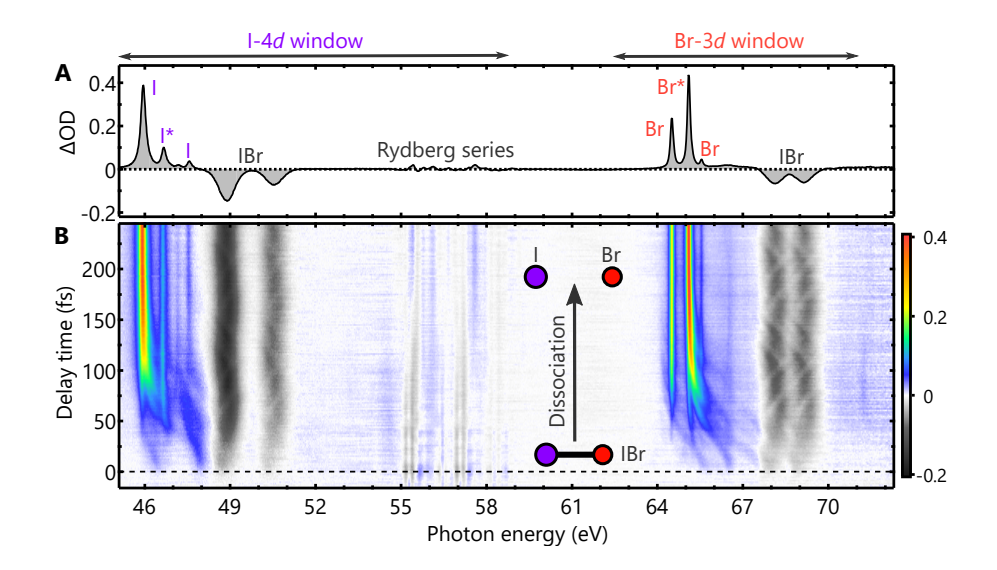
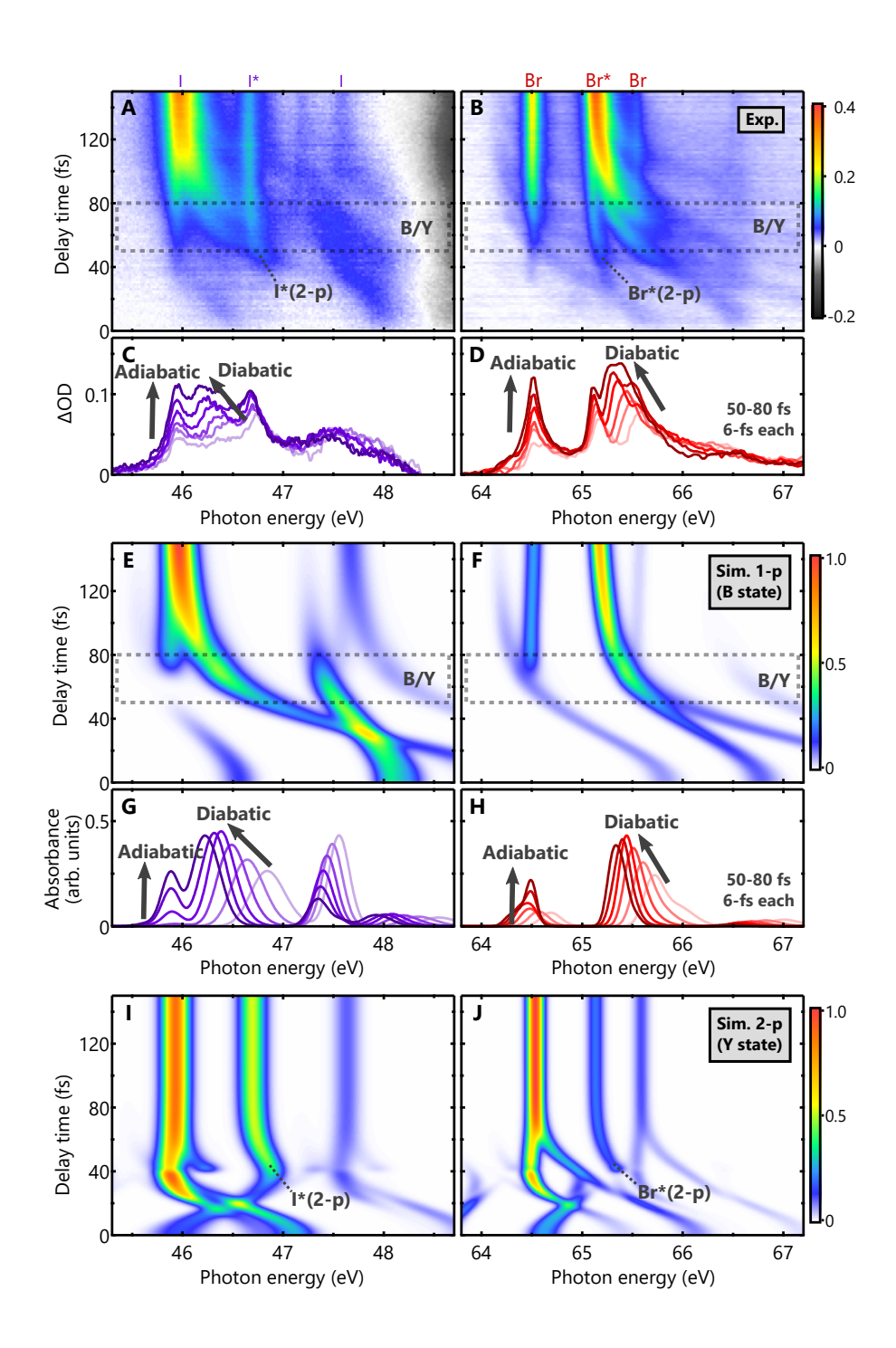


Fig 2: Core-level transient absorption spectra of IBr. (A) Transient absorption spectrum of the dissociation products recorded in the 215-245 fs delay-time range. (B) Delay-time resolved transient absorption spectra. At delay time zero, the visible-pump pulse initiates the dissociation processes, and excited-state signal (bright colors) as well as ground-state bleach (gray shades) emerge. The dissociation proceeds toward the positive delays.



**Fig 3: Experimental and simulated spectra of nonadiabatic dissociation dynamics.** (**A** and **B**) Experimental absorption spectra in the (A) I-4d and (B) Br-3d windows, respectively The temporal window for the B/Y avoided crossing is highlighted by dashed boxes. The I\* and Br\* signals originating from the two-photon process are also marked. (**C** and **D**) Absorption spectra taken from the experimental results at delay times of 50, 56, 62, 68, 74, and 80 fs. The assignments at the adiabatic and diabatic channels at the B/Y avoided crossing are denoted. (**E** to **H**) One-photon (1-p) simulation results shown for the comparison with the experimental results (A) to (D). (**I** and **J**) Two-photon (2-p) simulation results that reproduce the early-time emergences of the I\* and Br\* signals.

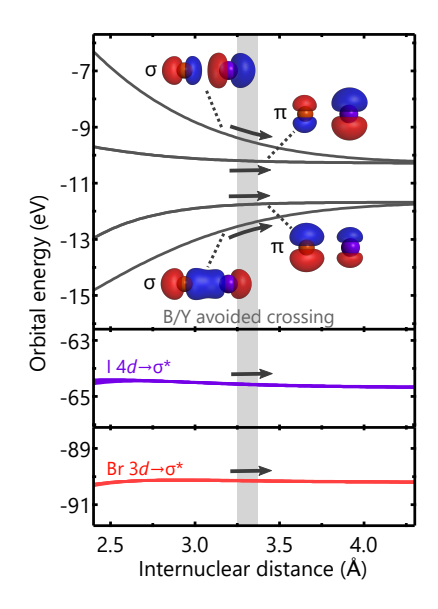


Fig 4: Orbital energies as a function of internuclear distance. The energy difference between the core and valence orbitals are closely tied to the observed absorption energies. Around the B/Y avoided crossing (gray area), the energies of the core orbitals and valence  $\pi/\pi^*$  orbitals are nearly invariant, whereas those of the  $\sigma/\sigma^*$  orbitals show increase/decrease versus internuclear distance. The displayed molecular orbitals are computed at R=3.3 Å.

#### **Materials and Methods**

#### 1. Experimental setup

Here we present the details of the experimental setup. Figure S1 illustrates the main components of the attosecond transient absorption beamline. A titanium:sapphire laser system (Femtopower Pro, Femtolasers GmbH) delivers a carrier-envelope-phase-stable near-infrared (NIR) femtosecond laser pulse (790 nm, 1.8 mJ, 1 kHz). The NIR pulse is focused into a stretched hollow-core fiber (1.5 m, 400  $\mu$ m, Few-cycle Inc.) filled with neon at 1.7 bar, and a broadband white-light pulse is generated through self-phase modulation. Spectral dispersion is compensated by a combination of twelve chirped mirrors (PC 70, Ultrafast Innovations GmbH), a 2-mm ADP crystal (United Crystals Inc.), and fused-silica wedges. As a result, a well-compressed few-cycle NIR pulse (700 nm, 3.5 fs, 0.8 mJ) is obtained (40). To produce a visible-pump pulse for the IBr experiment, the broadband beam splitter used for the conventional NIR-pump measurements is replaced by spectral separators for visible light (Layertec GmbH). The spectral separator reflects the visible component of the input pulse (95%, < 540nm), while it transmits the NIR component (95%, > 580 nm). To increase the spectral filtering, two spectral separators are used. Temporal characterization of the visible pulse is conducted using a home-built setup for self-diffraction frequency-resolved optical gating (SD-FROG) (41, 42), and a temporal width (full width half maximum) of 8.1 fs is recorded (Fig. S1, inset). The transmitted NIR part of the beam is used for highharmonic generation in argon to produce the XUV-probe pulse. Since the visible component is removed from the transmitted NIR pulse, the pulse duration is elongated (> 4 fs) and isolation of attosecond pulses cannot be attained by amplitude gating alone. In order to obtain the shortest possible XUV pulse, a thin (85 µm) quartz plate and a zeroth-order quarter-wave plate are introduced for polarization assisted amplitude gating (43), and a relatively continuous XUV spectrum is obtained (Fig. 1C). The visible-pump pulse and the XUV-probe pulse are combined at a hole mirror, and then they are reflected by a gold-coated toroidal mirror into an absorption gas cell (4-mm path length) filled with a gaseous IBr sample. A 300-nm aluminum filter is placed after the gas cell to block the visible pulse while it transmits the XUV pulse. The spectrum of the transmitted XUV pulse is recorded by an XUV spectrometer that consists of a concave grating (Hitachi 010-0640) and an XUV camera (Princeton Instruments, PIXIS 400). The spectral resolution is  $\sim 20$  meV in the I-4d window ( $\sim 50$  eV), and  $\sim 30$  meV in the Br-3d window ( $\sim 65$  eV). The IBr sample (Sigma-Aldrich, 98% purity) is heated at 60 °C to achieve high enough vapor pressure (8 Torr) for the transient absorption measurements. To prevent the exhaust line from getting corroded, a liquid-nitrogen trap is placed behind the turbomolecular pumps to capture the exiting IBr vapor.

#### **Supplementary Text**

#### 2. Effects from thermal decomposition of IBr

This result indicates that the signals in the Br-3d window are almost exclusively from IBr, but the I-4d window possibly contains the contribution from the I<sub>2</sub> molecule. The visible-absorption band of I<sub>2</sub> mainly consists of the transition to the B( $^3\Pi^u_{0^+}$ ) state. In contrast to the B( $^3\Pi^u_{0^+}$ ) state of IBr where the absence of the g-u symmetry enables the formation of the B/Y avoided crossing, the B( $^3\Pi^u_{0^+}$ ) state of I<sub>2</sub> is is free of such a curve crossing and is not predissociative. The dissociation energy for the associated I( $^2P_{3/2}$ ) + I\*( $^2P_{1/2}$ ) asymptote is  $\sim 2.5$  eV (46), which is higher than the center photon energy of the visible-pump pulse ( $\sim 2.3$  eV). Therefore, the signals from the I<sub>2</sub> molecule are expected to be mostly nondissociative. Experimentally, comparison between the experiments and simulations shows good agreement both in the I-4d and Br-3d windows (Fig. 3). Furthermore, in the vibrational-coherence signals from the ground-state bleach signals, the same oscillation patterns are observed both in the I-4d and Br-3d windows (see Figs. S3A-C in the next section). Overall, although we cannot completely eliminate the possible contributions from I<sub>2</sub>, the experimental evidences show the main experimental findings of the IBr-photodissociation dynamics are unaffected.

#### 3. Overtone excitation of vibrational wave packets in neutral ground state

In the experiments, the signature of vibrational coherences formed in the neutral ground state of IBr is observed. Here we provide a qualitative analysis of this finding. Additional experiments and analyses are underway in our group.

Figures S3A and B show the ground-state bleach signals in the I-4d and Br-3d windows, respectively. The color scale is reversed from Figs. 2 and 3 such that the negative  $\Delta OD$  signals are more distinguishable. The isotropic average of the vibrational frequencies of the  $X(^1\Sigma_{0^+})$  state is  $\omega_e=267.7~{\rm cm}^{-1}$  and  $\omega_e x_e=0.82~{\rm cm}^{-1}$  (30), which corresponds to an oscillation period of  $T=125.4~{\rm fs}$ . Oscillation patterns at this fundamental period as well as unique nodal structures are observable in the experimental results. Comparison among the different core-orbital windows is made by calculating the center-photon energies as a function of delay time (Fig. S3C). The same oscillation patterns are repeated in all four windows, which indicates that the contributions from  $I_2$  and  $I_2$  are insignificant. There have been a few experimental and theoretical reports on characterization of vibrational coherences created after strong-field ionization (31,32,47). In the latest study on methyl iodide (CH<sub>3</sub>I) (32), multiple frequency patterns were observed corresponding to the different vibrational modes of the molecule. However, in the present case, there is only one vibrational mode (I-Br stretch), and it is suggested that the observed nodal structures are a result of overtone excitations.

To obtain direct insights into the observed vibrational coherences, we perform quantum wave-packet simulations of the absorption signals. The electronic structures of the valence and core-excited states are computed by the SO-GMC-QDPT method (the details will be described in a later section). The ground  $X(^1\Sigma_{0^+})$  state has a main configuration of [2440] ([pqrs] refer to the valence electronic configuration of  $[\sigma^p\pi^q\pi^{*r}\sigma^{*s}]$ ) and is probed by the core-level transitions to the  $\sigma^*$  orbital. Therefore, only the core-excited states with a single-excited configuration of [2441] need to be considered here (see Fig. S6). Five electronic states (one ground state and four core-excited states) are included in the simulations, and their potential energy curves are shown in Fig. S3D. For the purposes of the wave-packet estimate, the transition dipole moments between the valence and core-excited states are assumed to be independent of the internuclear distance over a small range of the vibration, and the values are chosen as an average of the computed results at R=2.48 Å.

The time evolution of the nuclear wave packet is computed by numerically solving the time-dependent Schrödinger equation,

$$i\frac{\partial}{\partial t}\Psi = H\Psi. \tag{1}$$

Equations are expressed in atomic units ( $\hbar = 1$ ) unless otherwise specified. The Hamiltonian of the system is given by

$$\boldsymbol{H}(R,t) = -\frac{1}{2m} \frac{\partial^2}{\partial R^2} + \boldsymbol{V}(R) - \frac{i\boldsymbol{\Gamma}}{2} + E_{XUV}(t,\tau)\boldsymbol{\mu}, \tag{2}$$

where V is a matrix for the potential energies,  $\Gamma$  is a matrix for the finite lifetimes of the core-excited states,  $E_{\rm XUV}$  is an electric field of the XUV probe pulse arriving at a delay time  $\tau$ , and  $\mu$  is a matrix for the transition dipole moments. The lifetimes of the core-excited states are set as  $\Gamma=150~{\rm meV}$  (or 4.4 fs). The XUV pulse is approximated as a 100-as Gaussian pulse with a center photon energy of 60 eV. The choice of the XUV pulse does not affect the simulation results, and the present parameters are chosen such that both the I-4d and Br-3d windows are sufficiently covered. The time evolution of the non-Hermitian Hamiltonian is computed by the short-iterative Arnoldi method (48) at a step size of 5 as. In order to calculate the core-to-valence absorption strengths at each probe timing, the time-dependent dipole moment  $\mu(t) = \langle \Psi(t) | \mu | \Psi(t) \rangle$  and the probe electric field  $E_{\rm XUV}(t)$  are first Fourier-transformed into the frequency domain, and then converted into a generalized absorption cross section  $\sigma(\omega)$  using the following equation (49),

$$\sigma(\omega) \propto \omega \operatorname{Im} \left[ \frac{\mu(\omega)}{E_{\text{XUV}}(\omega)} \right].$$
 (3)

The visible excitation step is not explicitly considered; instead, vibrational wave packets in the ground state are approximated to be launched instantly at t=0. The probability distributions of the vibrational eigenstates are shown in Fig. S3E. The populations among the vibrational levels are arbitrarily chosen in a trial as n(v=0): n(v=1): n(v=2) = 0.7: 0.2: 0.1, which are found to qualitatively well reproduce the experimental results. The relative phases of the vibrational eigenstates are defined such that at t=0 the peak of the population is at the inner turning point of the potential.

Simulated absorption spectra are shown in Figs. S3E and F for the I-4d and Br-3d windows, respectively. The oscillation patterns as well as the nodal structures are reproduced in the simulations; without the population in the v=2 level, the nodal structures are unobserved (not shown here). It is of great interest to pursue more quantitative analysis of the populations and phases of the vibrational wave packets, which will provide insights about excitation mechanisms such as Raman and Lochfraß (32).

#### 4. Broadband-NIR pump transient-absorption results

In the experiments, a filtered femtosecond visible pulse is used to excite the lowest absorption band of IBr. Here we include supplementary experimental results of attosecond transient absorption spectroscopy where the full broadband-NIR pulse is used for the excitation. The main purpose is to demonstrate the importance of the spectral filtering to suppress ionization effects and to resonantly excite the visible-absorption band of interest. The XUV probe pulse is nearly identical to the one in the visible-excitation experiments except that

the spectrum is slightly more continuous and broader due to the shorter temporal width of the NIR-driver pulse for high-harmonic generation.

Figure S4 shows the broadband-NIR-pump results measured at a peak-field intensity of  $1 \times 10^{14}$  W/cm<sup>2</sup>. The pulse duration is near Fourier-transform limited at 3.5 fs (40). A transient absorption spectrum of the dissociation products is shown in Fig. S4A. The broadband-NIR spectrum contains the same visible-light components as in the femtosecond visible light, and it is able to excite the same neutral visible-band dynamics. A small fraction of the I<sup>+</sup> ion is produced, but all the rest of the spectral changes are the neutral atomic fragments. Therefore, the dissociation processes in the neutral excited states are certainly induced. Figure S4B shows the overview of the delay-dependent transient absorption spectra, and Figs. S4C and D show the results in the I-4d and Br-3d windows, respectively. Some of the signals resemble those observed in the visible-excitation results (Figs. 3A and B), ensuring the reproducibility of the main experimental findings.

However, the product ratio of Br\*/Br = 0.8 calculated from the XUV absorption spectrum (Fig. S4A) significantly deviates from the reference value (Br\*/Br = 3.0, 525-nm excitation) (26), indicating significant contributions from the multiphoton excitation and dissociative ionization. In the delay-dependent spectra (Figs. S4C and D), the signals from the B/Y avoided crossing are overwhelmed by those from the other dissociation channels occurring on a shorter time scale. These results lead to a conclusion that even though the broadband-NIR pulse is able to excite the targeted visible-band dynamics, multiphoton excitation and ionization are inevitably induced to an excessive extent.

#### 5. Details of the SO-GMC-QDPT calculations

Here we describe the calculation methods of the valence and core-excited electronic structures of IBr. The code for spin-orbit general multi-configurational quasi-degenerate perturbation theory (SO-GMC-QDPT) is implemented in the developer version of the GAMESS-US program package (33, 50). In all calculations, model-core potentials and basis sets of triple-zeta quality (MCP-TZP) (51, 52) are used. Calculation of core-excited electronic structures with SO-GMC-QDPT is also described in our recent publication (34).

First, a Hartree-Fock calculation is performed at R=2.48 Å, and the resultant molecular orbitals are used as an initial input for the subsequent multi-configurational self-consistent field (MCSCF) calculations. Active spaces are created based on the occupation-restricted multiple active-space (ORMAS) scheme. A valence-active space consists of the I-5p and Br-4p orbitals containing 10 electrons in 6 orbitals. A core-active space consists of the I-4d and Br-3d orbitals containing 20 electrons in 10 orbitals. The valence active space is

taken to be a complete active space, i.e., full excitations are allowed within this space. From the core-active space, single excitations into the valence-active space are allowed, which mimic the Br-3d and I-4d core-tovalence excitations. A total of 186 states are included in the state-averaging calculations: 66 states from the valence states associated with the I + Br,  $I^+$  + Br $^-$ , and  $I^-$  + Br $^+$  asymptotes, 60 states from the I-4d coreexcited states associated with the  $I(^2D)$  +  $Br(^2P)$  asymptote, and 60 states from the Br-3d core-excited states associated with the  $I(^2P) + Br(^2D)$  asymptote. In order to accurately account for the spin-orbit couplings in the four core and valence orbitals (I-4d, I-5p, Br-3d, and Br-4p), four empirical parameters (two effective nuclear charges, and two constant scaling factors) are manually optimized as follows. First, effective nuclear charges of  $Z_{
m eff}=71.37$  and 41.40 are used for the I and Br atoms, respectively, to reproduce the spin-orbit splittings in the I-5p and Br-4p orbitals. Second, the spin-orbit coupling matrices between the I-4d and Br-3d orbitals are scaled down by factors of 0.577 and 0.665, respectively, to reproduce the spin-orbit splittings in the I-4d and Br-3d orbitals. These optimizations are performed once at an asymptotic limit (R = 10.00 Å), and the same values are used throughout the internuclear distances. In addition, constant energy shifts of +0.16 eV and +0.38 eV are added to the I-4d and Br-3d core-excited potentials, respectively, to reproduce the experimental I  $4d \rightarrow 5p$ and Br  $3d \rightarrow 4p$  transitions. These energy shifts and scalings of the spin-orbit matrices are necessary because the basis sets and pseudopotentials are optimized for the atomic ground states, not for core-excited states.

#### 6. Valence electronic structure of IBr

Here we present the calculation results for the valence electronic structure of IBr. Evaluation of the calculated potentials is given by comparing the spectroscopic parameters with literature values. Excitation pathways with the visible-pump pulse are also discussed based on the calculated transition energies and transition dipole moments.

The potential energy curves for the five lowest  $\Omega=0^+$  states and six lowest  $\Omega=1$  states are shown in Fig. S5A. Each state is labeled with the  $\Omega$  value and energy order (e.g. IV(1) means the fourth lowest state with  $\Omega=1$ ). Within the dipole selection rule for linear molecules, the parallel transition ( $\Delta\Omega=0$ ) and perpendicular transition ( $\Delta\Omega=\pm1$ ) are allowed by one-photon excitations. Also,  $0^+\leftrightarrow 0^-$  is prohibited. Therefore, the excited states that are optically accessible from the ground  $X(^1\Sigma_{0^+})$  state are restricted to those with  $\Omega=0^+$  and 1, and thus the states with  $\Omega=0^-$  and 2 need not be considered further.

The spectroscopic parameters (equilibrium internuclear distance  $R_e$ , harmonic frequency  $\omega_e$ , anharmonicity  $\omega_e x_e$ , and adiabatic excitation energy  $T_e$ ) are evaluated for the bound electronic states, i.e.,  $X(^1\Sigma_{0^+})$ ,  $A(^3\Pi_1)$ ,

and  $B(^3\Pi_{0^+})$ . The results are summarized in Table S1. The vibrational energies are calculated based on the eigenvalues of the Hamiltonian for nuclear motion, and then fitted with a linear function to extract the harmonic frequency  $(\omega_e)$  and anharmonicity  $(\omega_e x_e)$ . The equilibrium internuclear distance  $(R_e)$  and the adiabatic excitation energy  $(T_e)$  are obtained by fitting the energies with a Morse potential. The isotope used for the calculations is  $^{127}I^{81}Br$ . Overall, good agreement with literature values is obtained (30, 36, 53, 54), indicating the capability of the calculated results to provide robust description of the valence electronic states.

The visible absorption band of IBr consists of the transitions into the three lowest excited states,  $A(^1\Pi_1)$ ,  $B(^3\Pi_{0^+})$ , and  $C(^1\Pi_1)$  (55). Figure S5B shows the transition dipole moments (TDMs) calculated between the ground  $X(^1\Sigma_{0^+})$  state and the excited-state manifold. For the three lowest excited states, the vertical excitation energies as well as transition dipole moments at R=2.46 Å are shown in brackets. It is clear that the  $B(^3\Pi_{0^+})$  state has the largest transition dipole moment (0.33 au) broadly around the Franck-Condon region. The  $C(^1\Pi_1)$  state lies energetically too high (2.80 eV) for the visible-excitation light ( $\sim 2.3$  eV), and the transition dipole moment for the  $A(^1\Pi_1)$  state is very small (0.02 au) in comparison to the  $B(^3\Pi_{0^+})$  state. These results lead to the well-established conclusion that the  $X \to B$  transition is the dominant pathway in the visible excitation.

Compared to the  $X \to B$  transition in the visible absorption band, literature on the possible secondary excitation from the  $B(^3\Pi_{0^+})$  state to the higher state manifold is scarce. In a theoretical study by Patchkovskii (35), large transition dipole moments associated with the  $B \to Y$  transition were calculated. In Fig. S5C, the transition dipole moments calculated from the excited  $B(^3\Pi_{0^+})$  state to the other excited states are shown. Indeed, the transition dipole moment to the  $Y(0^+)$  state is large (1.37 au) in the Franck-Condon region, and the excitation energy (2.14 eV) falls in the coverage of the visible-pump pulse. The  $Z(0^+)$  state also has a large transition dipole moment (0.65 au) with a slightly higher excitation energy (2.30 eV), and thus its contribution is possible. The excited  $IV(0^+)$  state has a large transition dipole moment (0.61 au), but the excitation energy is too high (3.57 eV) to be reached by the visible-pump pulse. Based on the experimental spectrum of the visible-pump pulse (Fig. 2B) and the calculated transition dipole moments, the transition probabilities from the  $B(^3\Pi_{0^+})$  state are estimated to be Y:Z=4:1. Accordingly in the two-photon simulations shown in Figs 3I and J, only the most important contribution from the  $Y(0^+)$  state is considered.

#### 7. Core-excited electronic structures of IBr

Here we present an analysis of the core-excited electronic structure of IBr. Figures S6A and B show the spin-orbit-free Br-3d and I-4d core-excited states, respectively, calculated at the level of GMC-QDPT. Figures S6C

and D show the results including the spin-orbit couplings, calculated at the level of SO-GMC-QDPT.

We first look at the spin-orbit-free potentials. In the Br-3d core-excited states (Fig. S6A), the electronic configurations that arise from the  $I(^2P)$  +  $Br(^2D)$  asymptote are  $[3d^9][2441]$  and  $[3d^9][2432]$ , and these configurations give rise to two groups of potentials in the Franck-Condon region. The I-4d core-excited states exhibit similar structure as in the Br-3d core-excited states (Fig. S6B). The lower group of the potentials have a main configuration of  $[4d^9][2441]$  in the Franck-Condon region, which converge to  $[4d^9][1442]$  toward the asymptotic limit. The higher group of the potentials belongs to the  $[4d^9][2342]$  configuration. The variation in the lower group is because the  $I(^2D)$  +  $I(^2P)$  asymptote corresponds to the  $I(^4D)$  and  $I(^4D)$  and  $I(^4D)$  and  $I(^4D)$  configurations in the asymptotic limit.

We then turn to the spin-orbit coupled potentials (Figs. S6C). In the Br-3d core-excited states (Fig. S6C), the potentials exhibit doublet splitting in the  $[3d^9][2441]$  configuration, and quartet splitting in the  $[3d^9][2432]$  configuration. The origin of the splittings that is common to the two configurations is the spin-orbit coupling in the Br-3d core hole (solid vertical arrows). The other factor that takes effect for the  $[3d^9][2432]$  configuration is the spin-orbit coupling in the vacancy of the  $\pi^*$  orbital (dashed vertical arrows). As a result, the core-excited potentials comprise six potentials in the Franck-Condon regime. Similar arguments can be applied for the I-4d core-excited states (Fig. S6D). The larger splittings common to the two configurations (solid vertical arrows) originate from the spin-orbit coupling in the I-4d core hole, and the smaller splittings (dashed vertical arrows) are due to the vacancy in the  $\pi$  orbital.

#### 8. Internuclear-distance dependent core-to-valence absorption strengths

Here we present the core-to-valence absorption strengths as a function of internuclear distance calculated for the four valence states involved in the visible-pump experiments. Figure S7A is the results for the ground  $X(^1\Sigma_{0^+})$  state, and the corresponding potential energy curve is highlighted by a thick black curve in Fig. S7E. Similarly, Figs. S7B, C, and D show the calculated absorption strengths for the excited  $B(^3\Pi_{0^+})$ ,  $Y(0^+)$ , and  $Z(0^+)$  states, respectively, and Figs. S7F, G, H highlight the corresponding potential energy curves, respectively. The transition energies and transition dipole moments are obtained from the SO-GMC-QDPT results. The plotted absorption strengths are computed by summing the oscillator strengths convoluted with Gaussian broadenings of 200-meV for the I-4d signals, and 120-meV for Br-3d signals.

The  $X(^1\Sigma_{0^+})$  [2440] state is probed through the  $nd \to \sigma^*$  transitions (Fig. S7A). Here, nd represents the I-4d and Br-3d orbitals. The absorption signals shift to lower photon energy as the internuclear distance

increases. This is a result of the decrease in the bond order after the  $nd \to \sigma^*$  transitions. The acute variation between the internuclear distance and transition energy is utilized in the characterization of the vibrational coherences in the ground  $X(^1\Sigma_{0^+})$  state, as was demonstrated in the experiments (Fig. S3).

The excited  $B(^3\Pi_{0^+})$  has a main configuration of [2431] in the Franck-Condon region, and it is probed through the  $nd \to \sigma^*$  and  $nd \to \pi^*$  transitions (Fig. S7B). The absorption signals shift to lower photon energy as the internuclear distance increases, as a result of the decrease in the bond order after the core-to-valence excitations. At the B/Y avoided crossing, the electronic character switches and the absorption signals immediately begin to look like the atomic  $^2P_{3/2} \to ^2D_{5/2,3/2}$  transitions.

The excited  $Y(0^+)$  and  $Z(0^+)$  states in the Franck-Condon region are probed through the  $nd \to \pi^*$  and  $nd \to \pi$  transitions (Figs. S7C, D). The  $nd \to \pi$  transitions induce the absorption signals to shift to higher photon energy as the internuclear distance increases, reflecting the bonding character of the  $\pi$  orbital. Overall, the absorption signals show complex behavior versus internuclear distance because the two states have multiconfigurational character, and there are inner  $(R_c = 2.2 \text{ Å})$  and outer  $(R_c = 2.8 \text{ Å})$  avoided crossings between the two states.

#### 9. Details of the nuclear wave-packet dissociation simulations

Here we provide the details of the simulation methods for the nonadiabatic nuclear wave-packet dynamics. The results are used to simulate the absorption signals shown in Fig. 3.

The Hamiltonian of the molecule including the nonadiabatic terms takes the form (56),

$$\boldsymbol{H}(R,t) = \left[ -\frac{1}{2m} \frac{\partial^2}{\partial R^2} + \boldsymbol{V}(R) \right] + \left[ -\frac{1}{m} \boldsymbol{D}_1(R) \frac{\partial}{\partial R} - \frac{1}{2m} \boldsymbol{D}_2(R) \right]. \tag{4}$$

Rotational motion of the molecule is not considered here. In Equation (4), R is the internuclear distance, and m is the reduced mass of the molecule. The atomic weights of the I and Br atoms are taken to be their isotopic averages of 126.904 and 79.904, respectively. The last terms in the bracket represent nonadiabatic interactions which are neglected within the Born-Oppenheimer approximation. The matrices  $D_1$  and  $D_2$  are first and second order nonadiabatic coupling terms that contain  $\langle \phi_i(R) | \frac{\partial}{\partial R} | \phi_j(R) \rangle$  and  $\langle \phi_i(R) | \frac{\partial^2}{\partial R^2} | \phi_j(R) \rangle$ , respectively.

Adiabatic potential energies are first computed by the SO-GMC-QDPT method from 2.00 Å to 5.00 Å with a step size of 0.01 Å. The grid points are evaluated by cubic spline interpolation and a finer grid space with a step size of 0.0025 Å is obtained. The grid space is further extended up to 6.50 Å to avoid the effects from

the reflection of the wave packets. The nuclear wave functions are expressed by sinc-DVR (57). The time propagation is performed using the short-iterative Lanczos method at a step size of 30 as.

The nonadiabatic coupling terms  $D_1$  and  $D_2$  are obtained from the diabatic coupling element  $V_{ij}$ , and the diabatic coupling element is obtained from the two-state diabatic crossing model (35, 58). The procedure is as follows. Near the curve crossing  $R_c$ , the energy difference between the two adiabatic states is given by

$$\Delta E = 2V_{ij}\sqrt{1 + \left(\frac{\Delta F}{2V_{ij}}\right)^2 (R - R_c)^2},\tag{5}$$

where  $\Delta F$  is the difference in the slopes of the diabatic potentials. The fitted results for the B/Y and Y/Z avoided crossings are listed in Table S2. Comparison with previous computational studies shows good agreement (35, 37). Assuming that the diabatic coupling element is constant in the vicinity of the curve crossing, the nonadiabatic coupling terms can be expressed as,

$$\left\langle \phi_i \left| \frac{\partial}{\partial R} \right| \phi_j \right\rangle = \frac{\Delta F V_{ij}}{4V_{ij}^2 + \Delta F^2 (R - R_c)^2}.$$
 (6)

In a simple case where only two electronic states interact, the first and second-order terms can be associated by (58),

$$\left\langle \phi_i \left| \frac{\partial^2}{\partial R^2} \right| \phi_j \right\rangle = \frac{\partial}{\partial R} \left\langle \phi_i \left| \frac{\partial}{\partial R} \right| \phi_j \right\rangle. \tag{7}$$

Finally, to determine the core-level absorption signals at each delay time, the computed nuclear wave packets are convoluted with the internuclear-distance dependent absorption signals (Fig. S7). Signals from the three valence states are taken as an incoherent summation.

#### 10. Results of the nuclear wave-packet dissociation simulations

Here we present the results of the nuclear wave-packet simulations. The state labels B, Y, and Z are given in the same way as in Figs. S7F, G, and H.

The time evolution of the nuclear wave packets for the one-photon process is shown in Figs. S8A and B. The initial wave packet is on the  $B(^3\Pi_{0^+})$  state (Fig. S8A), and at the B/Y avoided crossing ( $R_c=3.3~\text{Å}$ ) nonadiabatic population transfer occurs to the  $Y(0^+)$  state (Fig. S8B). Figure S8C shows the time evolution of the populations of the  $B(^3\Pi_{0^+})$  and  $Y(0^+)$  states. The time window from 50 fs to 80 fs, where the experimental signature of the B/Y avoided crossing is observed, is highlighted by blue shade. This window includes both non-avoided-crossing and avoided-crossing regimes.

The results for the two-photon process are shown in Figs. S8D to F. The initial wave packet is on the  $Y(0^+)$  state (Fig. S8E), and it soon ( $\sim 25$  fs) reaches the Y/Z avoided crossing ( $R_c = 2.8$  Å) and part of the population transfers to the  $Z(0^+)$  state. The wave packet further proceeds down the  $Y(0^+)$  potential and then ( $\sim 40$  fs) reaches the B/Y avoided crossing ( $R_c = 3.3$  Å).

#### References

- 1. G. A. Worth, L. S. Cederbaum, Annual Review of Physical Chemistry 55, 127 (2004).
- 2. B. G. Levine, T. J. Martínez, Annual Review of Physical Chemistry 58, 613 (2007).
- 3. M. P. Bircher, et al., Structural Dynamics 4, 061510 (2017).
- 4. L. D. Landau, Phys. Z. Sowjetunion 2, 46 (1932).
- 5. C. Zener, R. H. Fowler, R. Soc. London Ser. A 137, 696 (1932).
- 6. D. Polli, et al., Nature 467, 440 (2010).
- 7. T. Schultz, et al., Science **306**, 1765 (2004).
- 8. B. J. Sussman, D. Townsend, M. Y. Ivanov, A. Stolow, *Science* **314**, 278 (2006).
- 9. M. E. Corrales, et al., Nature Chemistry 6, 785 (2014).
- 10. S. R. Leone, et al., Nature Photonics 8, 162 (2014).
- 11. S. Takeuchi, et al., Science **322**, 1073 (2008).
- 12. M. C. E. Galbraith, et al., Nature Communications 8, 1018 (2017).
- 13. A. von Conta, et al., Nature Communications 9, 3162 (2018).
- 14. A. E. Boguslavskiy, et al., The Journal of Chemical Physics 148, 164302 (2018).
- 15. H. Timmers, et al. (Submitted).
- 16. H. J. Wörner, et al., Science **334**, 208 (2011).
- 17. J. Yang, et al., Science **361**, 64 (2018).
- 18. S. P. Neville, et al., Faraday Discuss. 194, 117 (2016).
- 19. S. P. Neville, M. Chergui, A. Stolow, M. S. Schuurman, *Phys. Rev. Lett.* **120**, 243001 (2018).
- 20. F. Krausz, M. Ivanov, Rev. Mod. Phys. 81, 163 (2009).

- 21. M. S. Child, R. B. Bernstein, The Journal of Chemical Physics 59, 5916 (1973).
- 22. M. S. Child, *Molecular Physics* **32**, 1495 (1976).
- 23. D. J. Seery, D. Britton, *The Journal of Physical Chemistry* **68**, 2263 (1964).
- 24. See Supplemental Material for more details.
- 25. T. Van Voorhis, et al., Annual Review of Physical Chemistry 61, 149 (2010).
- 26. E. Wrede, et al., The Journal of Chemical Physics 114, 2629 (2001).
- 27. L. Nahon, P. Morin, F. C. Farnoux, *Physica Scripta* **1992**, 104 (1992).
- 28. G. O'Sullivan, C. McGuinness, J. T. Costello, E. T. Kennedy, B. Weinmann, Phys. Rev. A 53, 3211 (1996).
- 29. L. Nahon, P. Morin, Phys. Rev. A 45, 2887 (1992).
- 30. R. E. Willis, W. W. Clark, The Journal of Chemical Physics 72, 4946 (1980).
- 31. E. R. Hosler, S. R. Leone, Phys. Rev. A 88, 023420 (2013).
- 32. Z. Wei, et al., Nature Communications 8, 735 (2017).
- 33. T. Zeng, The Journal of Chemical Physics **146**, 144103 (2017).
- 34. Y. Kobayashi, T. Zeng, D. M. Neumark, S. R. Leone, Structural Dynamics 6, 014101 (2019).
- 35. S. Patchkovskii, *Phys. Chem. Chem. Phys.* **8**, 926 (2006).
- 36. R. Li, et al., Journal of Quantitative Spectroscopy and Radiative Transfer 133, 271 (2014).
- 37. T. Matsuoka, S. Yabushita, The Journal of Physical Chemistry A 119, 9609 (2015).
- 38. M. Chergui, A. H. Zewail, *ChemPhysChem* **10**, 28 (2009).
- 39. P. M. Kraus, M. Zürch, S. K. Cushing, D. M. Neumark, S. R. Leone, *Nature Reviews Chemistry* 2, 82 (2018).
- 40. H. Timmers, et al., Opt. Lett. 42, 811 (2017).

- 41. R. Trebino, et al., Review of Scientific Instruments 68, 3277 (1997).
- 42. H.-T. Chang, et al., Opt. Lett. 41, 5365 (2016).
- 43. H. Timmers, et al., Optica 3, 707 (2016).
- 44. W. Evans, T. Munson, D. Wagman, J. Research Natl. Bur. Standards 55, 147 (1955).
- 45. J. Tellinghuisen, *The Journal of Chemical Physics* **76**, 4736 (1982).
- 46. J. I. Steinfeld, R. N. Zare, L. Jones, M. Lesk, W. Klemperer, *The Journal of Chemical Physics* **42**, 25 (1965).
- 47. A. D. Dutoi, S. R. Leone, *Chemical Physics* **482**, 249 (2017).
- 48. W. T. Pollard, R. A. Friesner, *The Journal of Chemical Physics* **100**, 5054 (1994).
- 49. M. Wu, S. Chen, S. Camp, K. J. Schafer, M. B. Gaarde, J. Phys. B 49, 062003 (2016).
- 50. M. W. Schmidt, et al., Journal of Computational Chemistry 14, 1347 (1993).
- 51. E. Miyoshi, Y. Sakai, K. Tanaka, M. Masamura, *Journal of Molecular Structure: THEOCHEM* **451**, 73 (1998).
- 52. M. Sekiya, T. Noro, Y. Osanai, T. Koga, Theoretical Chemistry Accounts 106, 297 (2001).
- 53. J. O. Clevenger, Q. P. Ray, J. Tellinghuisen, X. Zheng, M. C. Heaven, *Canadian Journal of Physics* **72**, 1294 (1994).
- 54. L. Selin, B. Soederborg, Ark. Fys. 21 (1962).
- 55. S. P. Sitkiewicz, et al., The Journal of Chemical Physics **145**, 244304 (2016).
- 56. M. Monnerville, J. Robbe, *The European Physical Journal D Atomic, Molecular, Optical and Plasma Physics* 5, 381 (1999).
- 57. D. T. Colbert, W. H. Miller, The Journal of Chemical Physics 96, 1982 (1992).
- 58. H. Lefebvre-Brion, R. W. Field, *The Spectra and Dynamics of Diatomic Molecules*, H. Lefebvre-Brion, R. W. Field, eds. (Academic Press, San Diego, 2004), pp. 87 231.

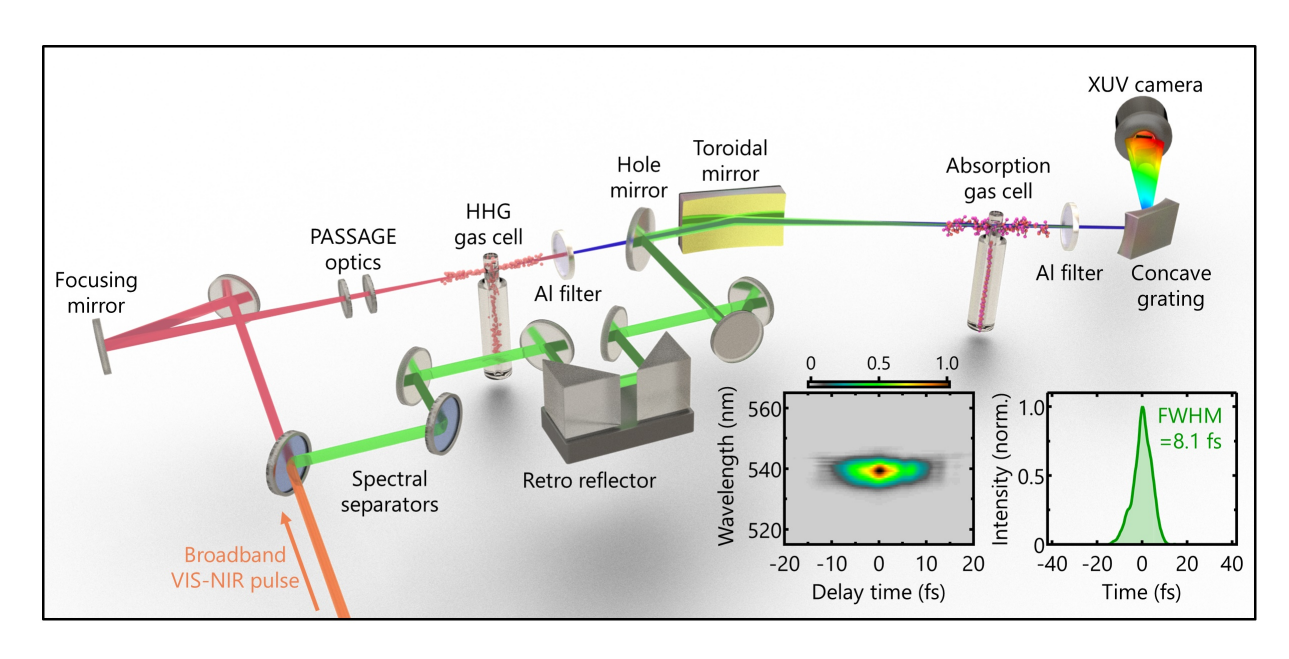


Fig S1: Illustration of attosecond transient absorption beamline. A broadband NIR laser pulse (orange beam) is split by spectral separators into the NIR components (red beam) and visible components (green beam). The NIR pulse drives the high-harmonic generation, which creates an attosecond XUV pulse (blue beam). A thin quartz plate and a zeroth-order quarter-wave plate (PASSAGE optics) are used for polarization assisted amplitude gating. An aluminum filter is used to remove the NIR driver pulse after the high-harmonic generation. The characterization of the visible pulse is performed with self-diffraction FROG. The insets show the measured FROG trace (left) and retrieved electric-field intensity (right). The visible pulse and the XUV pulse are combined at a hole mirror and are focused by a toroidal mirror into an absorption gas cell. The visible pulse is removed by another aluminum filter placed after the absorption gas cell. The transmitted XUV pulse is recorded by an XUV spectrometer.

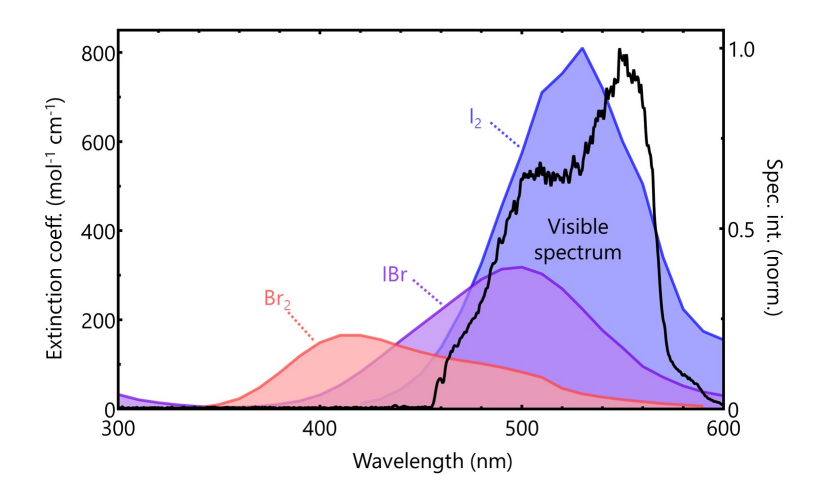


Fig S2: Absorption cross sections of IBr,  $I_2$ , and  $Br_2$ . The visible absorption cross sections are taken from (23) for IBr (purple area) and  $Br_2$  (red area), and from (45) for  $I_2$  (blue area). The spectrum of the visible-pump pulse is plotted as a black curve.

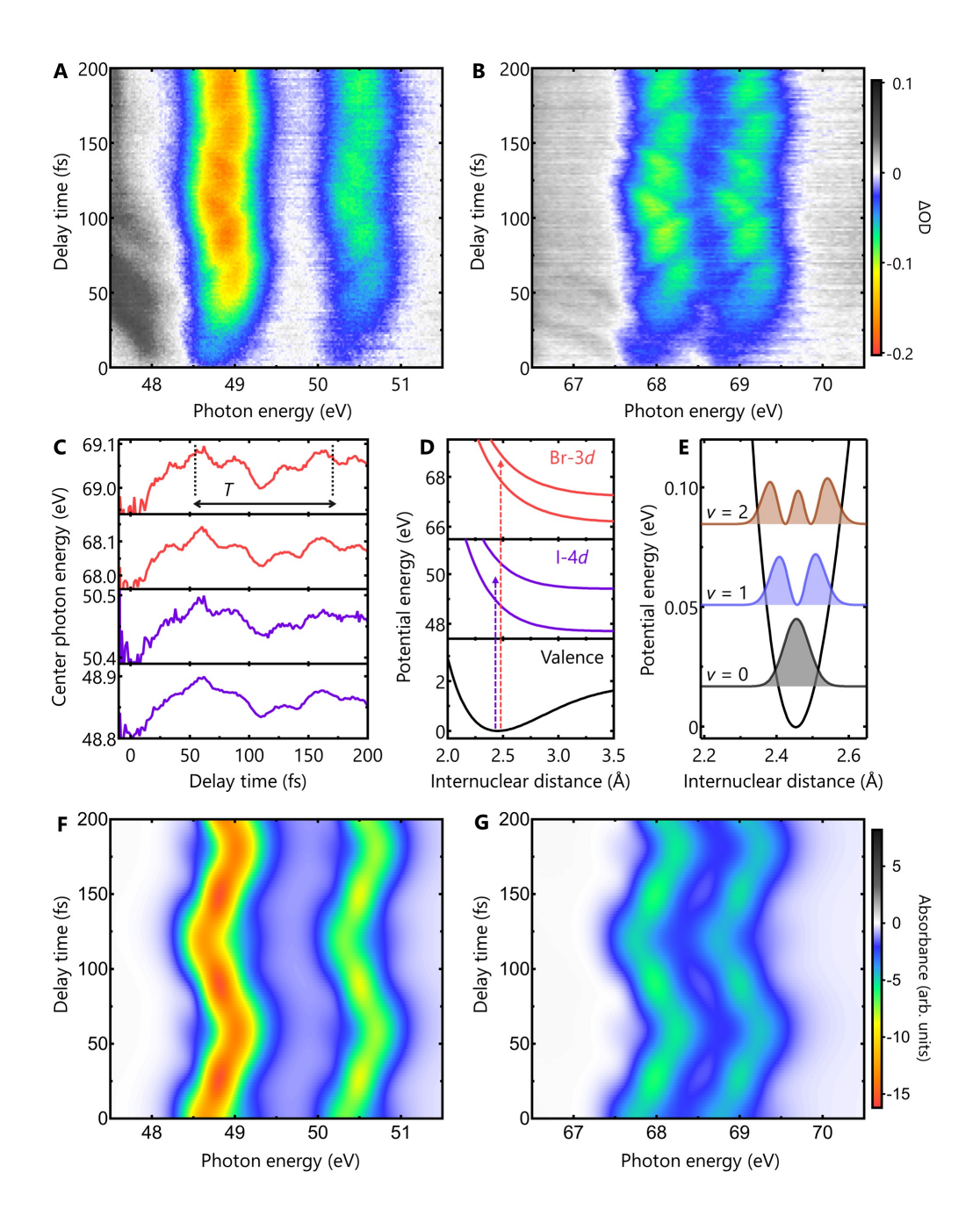


Fig S3: Vibrational coherences in ground-state bleach. (A,B) Experimental ground-state bleach signals in the (A) I-4d and (B) Br-3d windows. The color scale is reversed from Figs. 2 and 3 for clear visualization the negative  $\Delta$ OD signals. (C) Analysis of center-photon energies of the ground-state bleach signals. From top to bottom, the curves correspond to the Br-3 $d_{3/2}$ , Br-3 $d_{5/2}$ , I-4 $d_{3/2}$ , and I-4 $d_{5/2}$  windows. The fundamental vibrational period T for the ground  $X(^1\Sigma_{0^+})$  state is indicated by a double-head arrow. All four signals exhibit the same oscillation patters. (D) Potential energy curves employed in the numerical simulation of ground-state vibration signals. (E) Probability distribution of vibrational eigenstates of the ground  $X(^1\Sigma_{0^+})$  state. The three lowest v=0,1, and 2 levels are plotted, and they are included in the simulations. (F,G) Simulated transient absorption spectra in the I-4d and Br-3d windows showing the vibrational wave-packet dynamics.

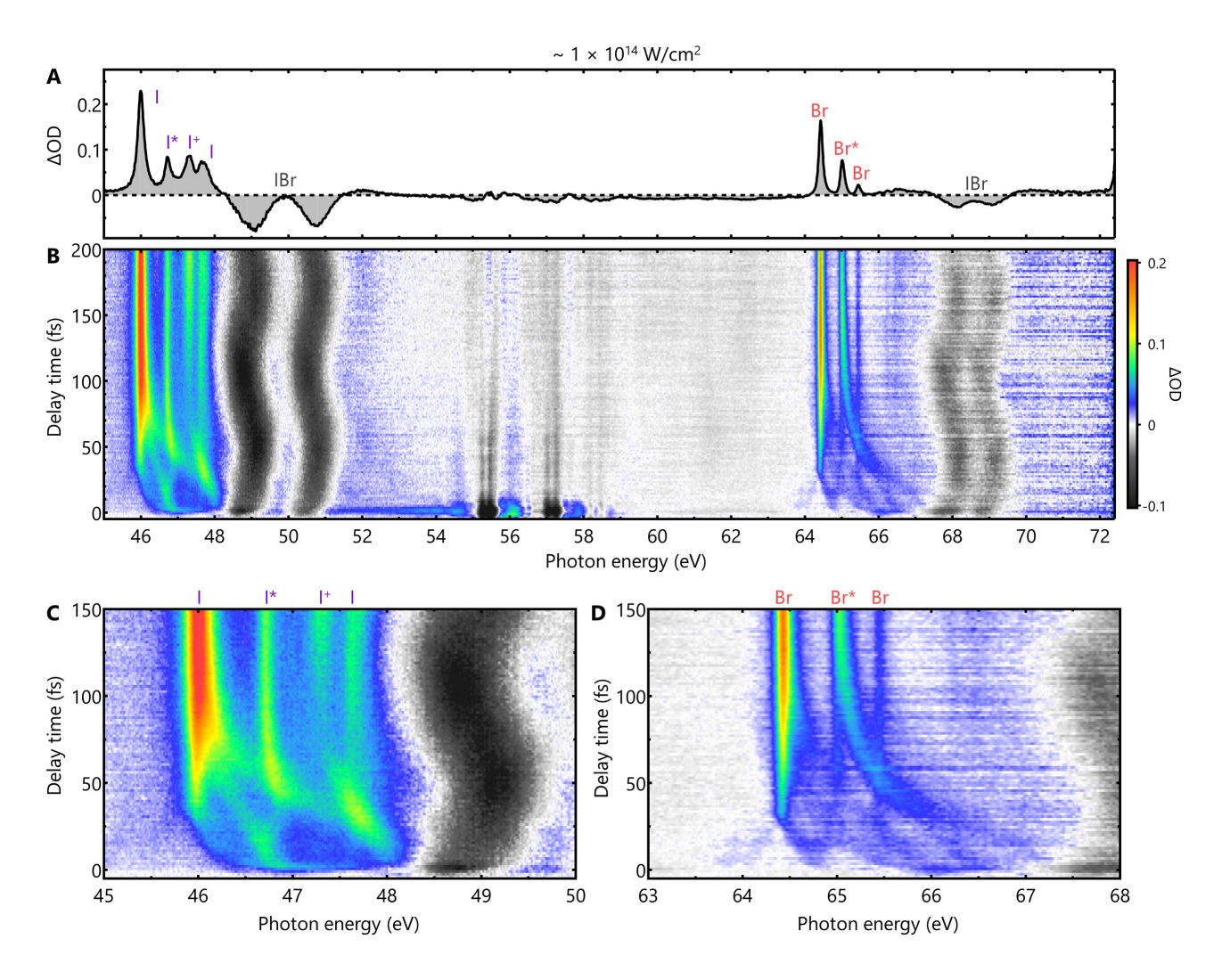


Fig S4: Broadband-NIR-pump transient absorption measurements of IBr. (A) A transient absorption spectrum of the dissociation products. Most of the signals are from the neutral atoms, but the product ratio of  $Br^*/Br = 0.8$  indicates multiphoton processes make significant contributions and alter the correct ratio. The ionic  $I^+$  signals is also evident, indicating the implication of ionization processes. (B) Overview of the delay-dependent transient-absorption spectra. (C and D) Transient-absorption signals in the (C) I-4d and (D) Br-3d windows.

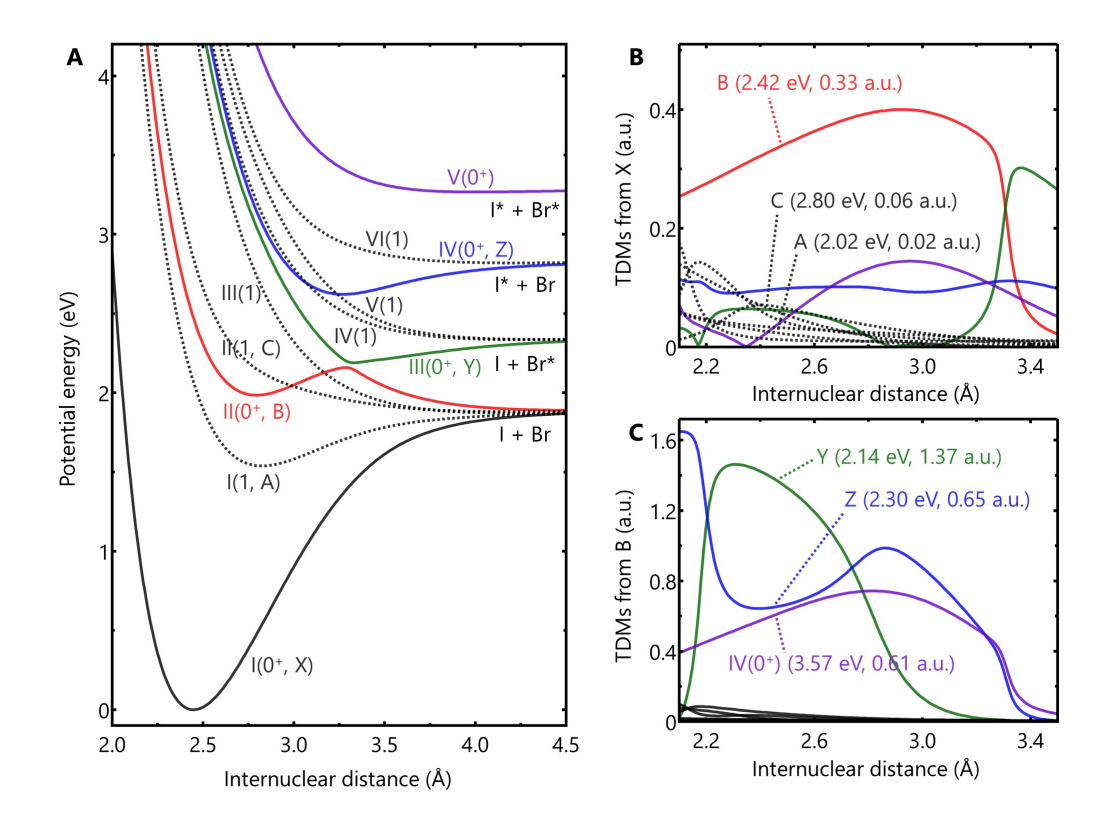


Fig S5: Valence potential energy curves and transition dipole moments of IBr. (A) Potential energy curves for the lowest five  $\Omega=0^+$  states and six  $\Omega=1$  states. Each state is labeled with the  $\Omega$  value and the order in energy. (B) Transition dipole moments (TDMs) from the ground  $X(^1\Sigma_{0^+})$  state. The values shown in brackets are the vertical excitation energy and transition dipole moment at R=2.46 Å. In the Franck-Condon region, the  $B(^3\Pi_{0^+})$  state has the largest transition dipole moment from the  $X(^1\Sigma_{0^+})$  state. (C) Transition dipole moments from the excited  $B(^3\Pi_{0^+})$  state to the other excited states. In the Franck-Condon region, the  $Y(0^+)$  and  $Z(0^+)$  states have large transition dipole moments.

State		$R_e$ (Å)	$\omega_e  (\mathrm{cm}^{-1})$	$\omega_e x_e \; (\text{cm}^{-1})$	$T_e  (\mathrm{eV})$
$X(^1\Sigma_{0^+})$	Expt. (30)	2.469	266.64	0.814	0
	Calc. (36)	2.482	265.7	0.72	0
	This work	2.448	267.9	0.66	0
$A(^3\Pi_1)$	Expt. (53)	2.858	134.22	0.983	1.53
	Calc. (36)	2.899	127.7	2.67	1.55
	This work	2.827	145.8	1.41	1.54
$B(^{3}\Pi_{0^{+}})$	Expt. (54)	2.83	142.0	2.6	2.00
	Calc. (36)	2.898	112.8	6.26	2.05
	This work	2.795	158.0	1.76	1.99

Table S1: Calculated and measured spectroscopic parameters of bound electronic states of IBr. The parameters included here are the equilibrium internuclear distance  $(R_e)$ , harmonic frequency  $(\omega_e)$ , anharmonicity  $(\omega_e x_e)$ , and adiabatic excitation energy  $(T_e)$ . The calculated results are compared with experimental data (30, 53, 54) and other theoretical work (36). The isotope used for calculation is  $^{127}I^{81}Br$ .

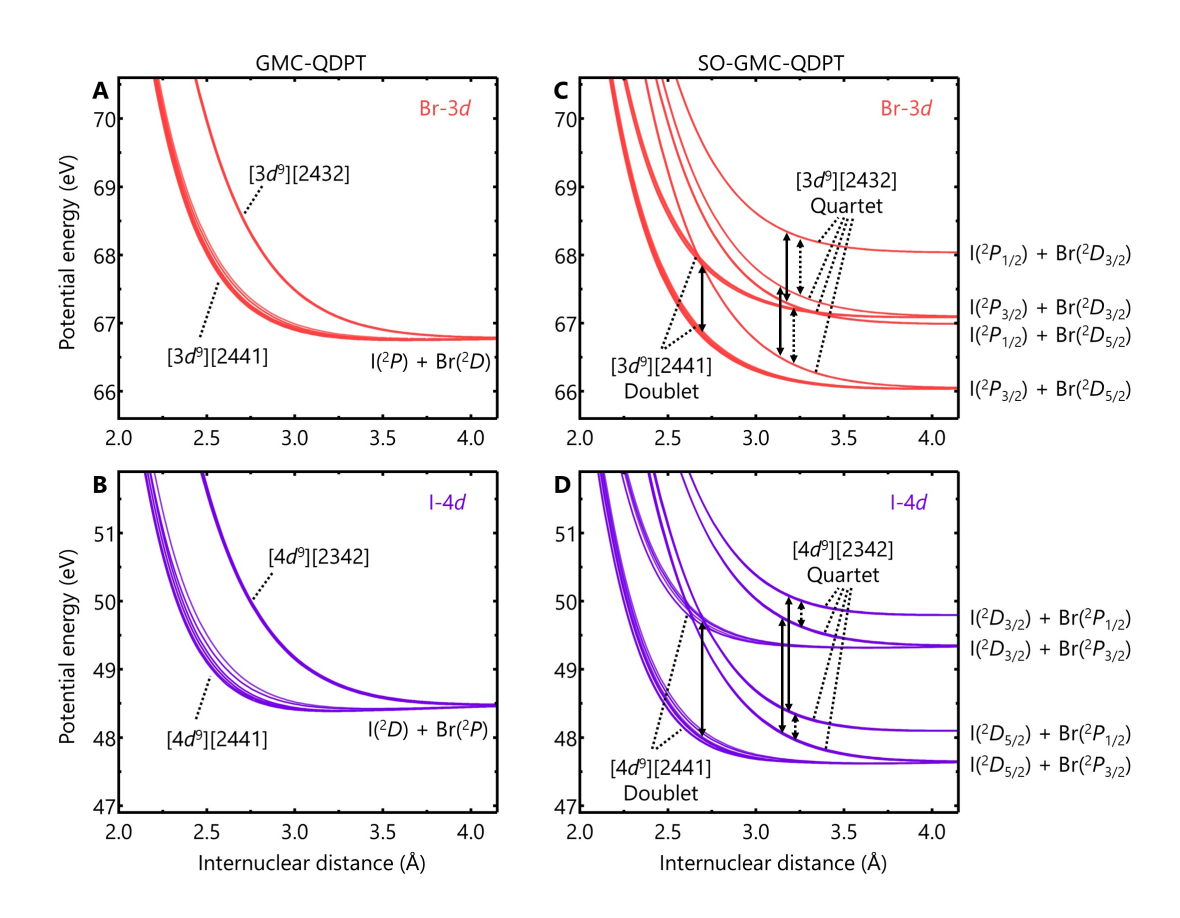


Fig S6: Core-excited potential energy curves of IBr. (A and B) Spin-orbit-free potentials of the (A) Br-3d and (B) I-4d core-excited states. (C and D) Spin-orbit-coupled potentials of the (C) Br-3d and (D) I-4d core-excited states. The spin-orbit couplings in the I-4d and Br-3d core holes (solid vertical arrows) cause doublet splittings in the  $[4d^9][2441]$  and  $[3d^9][2441]$  configurations, respectively. Additional splittings are caused by the spin-orbit coupling in the  $\pi$  and  $\pi^*$  orbital (dashed vertical arrows) to the  $[4d^9][2342]$  and  $[3d^9][2432]$  configurations, respectively.

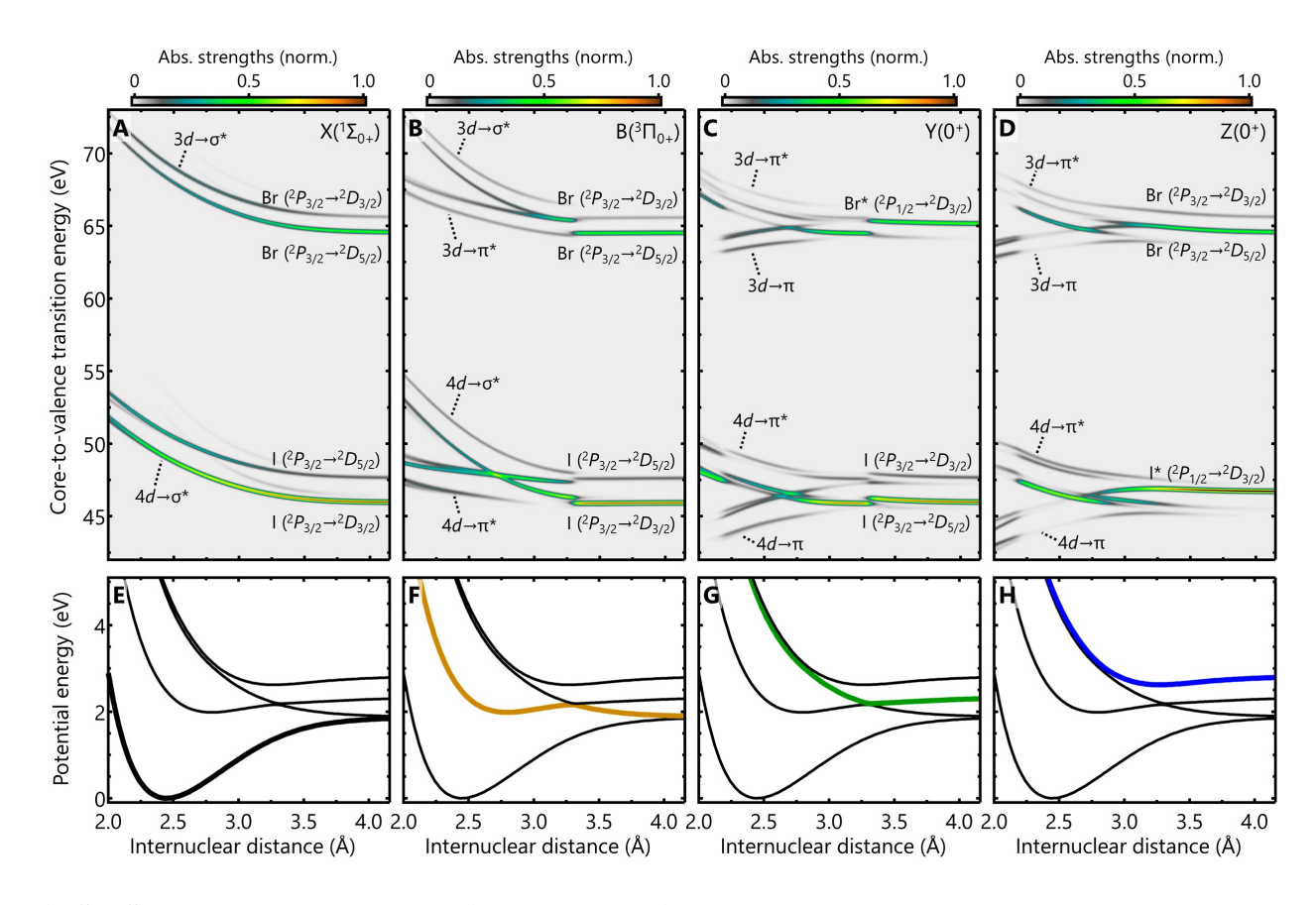


Fig S7: State-resolved XUV absorption strengths. (A to D) XUV absorption strengths calculated as a function of the internuclear distance. The results are from (A) the  $X(^1\Sigma_{0^+})$  state, (B)  $B(^3\Pi_{0^+})$  state, (C)  $Y(^3\Pi_{0^+})$  state, and (D)  $Z(^3\Sigma_{0^+})$  state. In the Franck-Condon regions, the states are probed through the  $nd \to \sigma^*, \pi^*, \pi$  transitions, depending on the occupations of the valence orbitals. In the asymptotic limits, the core-to-valence transitions converge to the I  $4d \to 5p$  and Br  $3d \to 4p$  series. (E to H) Overview of the valence potentials that highlight the targeted electronic states for the XUV absorption strengths.

State		$R_c$ (Å)	$V_{ij}$ (eV)	$\Delta F (\text{eV} \cdot \text{Å}^{-1})$
B/Y	Patchkovskii (35)	3.33	0.0153	1.02
	Matsuoka (37)	3.24	0.0164	1.06
	This work	3.31	0.0178	1.11
Y/Z	Patchkovskii (35)	2.87	0.0506	0.802
	Matsuoka (37)	2.82	0.0499	0.714
	This work	2.79	0.0503	0.636

Table S2: Avoided crossing parameters of the B/Y and Y/Z avoided crossings in IBr. Parameters for avoided crossings (crossing distance  $R_c$ , magnitude of nonadiabatic interaction  $V_{ij}$ , and the difference in the slopes  $\Delta F$ ) are computed by fitting the adiabatic energies to analytical expressions of a two-state diabatic model. The calculated results are compared with other computational work (35, 37).

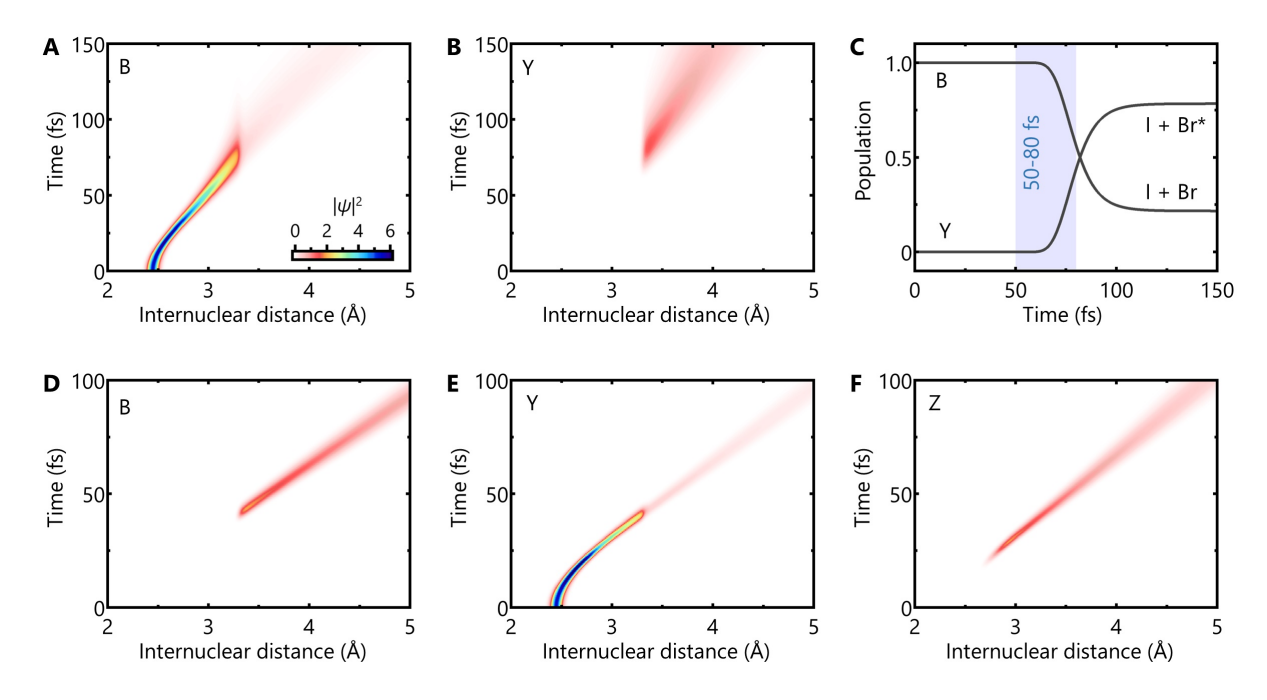


Fig S8: Nuclear wave-packets simulations for dissociation of IBr. (A and B) Simulation results for the one-photon process. State labels of B, Y, and Z are given the same way as in Figs. S7E, G, and H, respectively. The population densities ( $|\psi|^2$ ) are plotted for the (A) B( $^3\Pi_{0^+}$ ) state and (B) Y(0<sup>+</sup>) state. The initial wave packet is in the Franck-Condon region of the B( $^3\Pi_{0^+}$ ) state. (C) Population analysis for the one-photon process. When the wave packet reaches the B/Y avoided crossing, nonadiabatic population transfer occurs from the B( $^3\Pi_{0^+}$ ) to Y(0<sup>+</sup>) states. The time window from 50 fs to 80 fs is highlighted by blue shade. (D to F) Simulation results for the two-photon process. The population densities are plotted for the (D) B( $^3\Pi_{0^+}$ ) state, (E) Y(0<sup>+</sup>) state, and (F) Z(0<sup>+</sup>) state. The initial wave packet is in the Franck-Condon region of the Y(0<sup>+</sup>) state.